Insight into the improvement effect of the Ce doping into the SnO$_2$ catalyst for the catalytic combustion of methane

Cheng Liu[a], Hui Xian[b], Zheng Jiang[c], Lihua Wang[c], Jing Zhang[d], Lirong Zheng[d], Yisheng Tan[e], Xingang Li[a,*]

[a] Collaborative Innovation Center of Chemical Science & Engineering (Tianjin), Tianjin Key Laboratory of Applied Catalysis Science & Technology, School of Chemical Engineering & Technology, Tianjin University, Tianjin 300072, PR China
[b] School of Computer Science & Software Engineering, Tianjin Polytechnic University, Tianjin 300387, PR China
[c] Shanghai Synchrotron Radiation Facility, Shanghai Institute of Applied Physics, Chinese Academy of Sciences, Shanghai 201800, PR China
[d] Institute of High Energy Physics, Chinese Academy of Sciences, Beijing 100049, PR China
[e] State Key Laboratory of Coal Conversion, Institute of Coal Chemistry, Chinese Academy of Science, Taiyuan 030001, PR China

ARTICLE INFO

ABSTRACT

Herein, we report the performance of the catalytic combustion of methane over the Ce-doped SnO$_2$ catalysts. Doping with Ce increases the surface areas, decreases the crystallite sizes, and activates both the surface metal cations and surface oxygen species. Upon methane combustion, the surface Sn^{4+} cations are active sites, and the surface lattice oxygen plays an important role, as well. Kinetics results suggest that the activation energy (E_a) and pre-exponential factor (A) are determined by the reducibility and the area-specific quantity of the surface Sn^{4+} cations, respectively. The Sn$_{0.7}$Ce$_{0.3}$O$_2$ catalyst exhibits the highest area-specific rate because of its lowest E_a and relatively bigger A values. Its turnover frequency is five times higher, as compared with the SnO$_2$. The reaction pathways upon the Sn-rich catalysts (SnO$_2$ phase) follow the Mars–van Krevelen model, while they become more complex upon the Ce-rich ones (CeO$_2$ phase). Additionally, these SnO$_2$-based catalysts display the high water resistance.

© 2015 Elsevier B.V. All rights reserved.

1. Introduction

Methane, an economical and clean alternative to fuels, is widely used in power plants and new energy vehicles. However, the emission of the unburned methane will cause the serious greenhouse effect, which is approximately 25 times higher than carbon dioxide [1].

The catalytic combustion technology is a promising strategy to solve this problem by directly oxidizing methane into carbon dioxide and water. Noble metal based catalysts, such as platinum and palladium oxide, are effective in the catalytic combustion of methane [2–7]. Unfortunately, these catalysts are expensive and easily sintered at high operating temperatures. Therefore, upon this reaction there is a strong desire to design and synthesize non-noble metal catalysts, such as the reported Co$_{1-x}$Zr$_x$Cr$_2$O$_4$ [8], Ni$_{1-x}$Ce$_x$O$_2$ [9], Mn$_{1-x}$Ce$_x$O$_2$ [10], Mn$_{1-x}$Ni$_x$O$_2$ [11], and perovskite-type catalysts [12–14].

SnO$_2$-based materials have a lot of active surface oxygen species, as well as oxygen vacancies [15,16]. Consequently, they are regarded as one of potential alternatives for noble metal based catalysts in specific catalytic reactions, such as removal of nitrogen oxides [15,17] and CO oxidation [18,19]. It was reported that doping Cr [20] and Fe [21] into the SnO$_2$ catalyst could enhance the catalytic performance for methane combustion, probably due to the increased amount of the active oxygen species [20,21].

The CeO$_2$-based materials are well known because of their high oxygen storage capacity (OSC) [22–26], which are strongly related to the reversible Ce^{4+} ↔ Ce^{3+} redox reaction [22]. Attempts have been made to increase the amount of the Ce^{4+}/Ce^{3+} redox couples, and thus, to increase the OSC by substituting a part of Ce with other elements, such as Zr [22], Ti [23], Hf [24], and Sn [25,26]. Because the reversible Sn^{4+} ↔ Sn^{2+} redox process involves two-electron transfer, the OSC of the Ce$_{1-x}$Sn$_x$O$_2$ materials are higher than other CeO$_2$-based materials, such as Ce$_{1-x}$Zr$_x$O$_2$ [25,26] and Ce$_{1-x}$Ti$_x$O$_2$ [26]. Accordingly, the SnO$_2$–CeO$_2$ composite oxides may highly active as a potential oxidation catalyst [26].

Up to now, few reports deeply discussed the reaction mechanism upon the catalytic combustion of methane over the SnO$_2$-based catalysts. Additionally, the roles of surface oxygen

species, such as surface adsorbed oxygen and surface lattice oxygen, are still debated for the specific catalysts [27,28]. Despite of the expected high performance for the catalytic combustion of methane over the SnO_2–CeO_2 composite oxides, little attention has concerned this catalyst system. Herein, we report the catalytic performances of the $Sn_{1-x}Ce_xO_2$ composite oxides upon the methane combustion reaction. The $Sn_{1-x}Ce_xO_2$ catalysts were characterized by the X-ray diffraction (XRD), transmission electron microscopy (TEM), Raman spectroscopy, H_2 temperature-programmed reduction (H_2-TPR), O_2 temperature-programmed desorption (O_2-TPD), X-ray photoelectron spectroscopy (XPS), X-ray absorption fine structures (XAFS), and CH_4 temperature-programmed surface reactions (CH_4-TPSR). We intrinsically clarified the effect of the Ce dopant on the structures and physiochemical properties of the SnO_2-based catalysts. Thereafter, we determined the active species including the metal cations and oxygen species by combination of the above mentioned characterizations and kinetics measurements. On this basis, we calculated and analyzed the turnover frequency (TOF) data via the surface active metal cations. We discussed the factors determining the activation energy (E_a) and pre-exponential factor (A). The possible reaction mechanism, as well as the rate determining step, was proposed accordingly.

2. Experimental

2.1. Catalyst preparation

The SnO_2, CeO_2, and $Sn_{1-x}Ce_xO_2$ (x = 0.1, 0.3, 0.5, and 0.7) catalysts were prepared by the co-precipitation method. A stoichiometric amount of $SnCl_4 \cdot 4H_2O$ and/or $Ce(NO_3)_3 \cdot 6H_2O$ (Tianjin Guangfu Technology Development Co., Ltd.) was dissolved together in distilled water. Thereafter, an aqueous ammonia solution was added to the mixed solution by keeping pH 9. The obtained precipitates were filtered and washed with distilled water till no Cl^{-1} was detected by the $0.1\,mol\,L^{-1}$ $AgNO_3$ solution. The achieved powder was dried at 120 °C overnight, and then calcined at 650 °C in flowing air (300 mL min^{-1}) for 6 h. The resulting catalysts were named as $Sn_{1-x}Ce_xO_2$ (x = 0.1, 0.3, 0.5, and 0.7). The notation "x" represents the theoretical molar proportion of Ce to substitute Sn.

For comparison, the $0.1CeO_2/SnO_2$ catalyst with a molar ratio of Sn:Ce = 9:1 was prepared by the impregnation method. Briefly, the SnO_2 support prepared as described above was added to the $Ce(NO_3)_3$ aqueous solution under continuous stirring. The solution was heated at 80 °C to remove water. The formed powder was dried at 120 °C overnight, and then calcined at 650 °C in flowing air (300 mL min^{-1}) for 2 h.

2.2. Catalyst characterizations

The XRD tests were conducted with a Bruker D8-focus diffractometer, using Cu Kα (λ = 0.15418 nm) as the radiation source. The X-ray tube was operated at 40 kV and 40 mA. The lattice parameter was determined by the Rietveld refinement method using the JADE 6.0 software. The crystallite size (D) was calculated by Scherrer equation:

$$D = \frac{0.89\lambda}{(B\cos\theta)} \quad (1)$$

here, λ is the wavelength of the radiation source (0.15418 nm); B is the half width of the strongest diffraction peak in the radian unit; and θ is its diffraction angle.

The specific surface area (SSA) was determined by a N_2 physisorption experiment using an automatic gas adsorption system (NOVA 2000, Quantachrome Co.) at −196 °C.

The Raman spectra were recorded with a Raman spectrometer (in via Reflex, Andor) equipped with the NIR laser source (785 nm,

objective × 100) and TE-cooled CCD detector (Andor) with a resolution of 1.7–2 cm^{-1}.

TEM images were taken on a JEM-2100F (JEOL Co.) microscope operating at an acceleration voltage of 200 kV.

The temperature-programmed measurements were performed on a TPDRO (TP-5080, Xianquan Co.) instrument with a thermal conductivity detector (TCD). Before detection, the introducing gas was purified by a trap containing CaO and NaOH materials in order to remove H_2O and CO_2.

During the H_2-TPR operation, the sample (30 mg) was heated from room temperature (RT) to 900 °C with a rate of 10 °C min^{-1} in the 8% H_2/N_2 flow (30 mL min^{-1}). The amount of H_2 consumption was calibrated by the quantitative reduction of the standard CuO sample to the metallic copper.

For the O_2-TPD experiments, the sample (100 mg) was pretreated in pure O_2 (50 mL min^{-1}) from RT to 450 °C, and held for 0.5 h. After cooling to RT in pure O_2 (50 mL min^{-1}), the sample was purged by the He flow (30 mL min^{-1}) to get a stable TCD signal baseline, and then heated to 900 °C with a rate of 10 °C min^{-1}.

The CH_4-TPSR experiments were carried out with a fixed-bed reactor (i.d. = 4.5 mm). Prior to the CH_4-TPSR test, 200 mg of the sample was pretreated in the flow (50 mL min^{-1}) of pure N_2 or 20% O_2/N_2 from RT to 450 °C or 700 °C, and held for 0.5 h. After cooling to RT, the sample was heated to 900 °C in 5% CH_4/N_2 (50 mL min^{-1}) with a rate of 8 °C min^{-1}. The outlet gas was analyzed by an infrared gas analyzer (GXH-104C, Beifenpuqi Co.).

The XPS measurements were carried out on a Scienta ESCA-200 spectrometer with an accuracy of 0.3 eV. Al-Kα (1486.6 eV) was used as radiation source. The recorded spectra were calibrated by the characteristic binding energy (BE) peak at 284.6 eV belonging to the contaminant carbon in the 1s region.

The XAFS data of the Sn K-edge were collected with the fluorescence mode at 14W1 beamline of the Shanghai Synchrotron Radiation Facility (SSRF) with the storage ring energy of 3.5 GeV and the current of 250 mA. The XAFS measurements of the Ce L$_3$-edge were collected on the 1W1B beamline of Beijing Synchrotron Radiation Facility (BSRF) (120 mA and 2.5 GeV) with the fluorescence mode.

2.3. Catalytic tests

The methane combustion activities of all the catalysts were evaluated in a fixed-bed reactor (i.d. = 4.5 mm) by using 200 mg catalyst. Reaction conditions: feeding gas = 0.6 kPa CH_4, 19 kPa O_2, N_2 balance; and flow rate = 235 mL min^{-1}. The space velocity was about 80,000 h^{-1}. Prior to each measurement, the catalyst was activated at 500 °C for 2 h in 20% O_2/N_2 (150 mL min^{-1}). A thermocouple was inserted into the catalyst bed to monitor reaction temperatures. The data were collected at each temperature after the catalyst was stabilized for 0.5 h. The outlet gas was analyzed by the infrared analyzer as mentioned in the CH_4-TPSR experiments. The conversion of CH_4 ($X_{[CH_4]}$) was calculated as follows:

$$X_{[CH_4]} = \frac{\left(C_{[CO]} + C_{[CO_2]}\right)}{C_{[CH_4]}} \times 100\% \quad (2)$$

the $C_{[CO]}$ and $C_{[CO_2]}$ are the CO and CO_2 molar flows in the outlet gas, respectively, and the $C_{[CH_4]}$ is the CH_4 molar flow in the feeding gas.

2.4. Kinetics tests

The kinetics studies were conducted in the same fixed-bed reactor as mentioned in Section 2.3. Before the experiments, the internal and external diffusion limitations were eliminated (see Fig. S1). The tests were conducted at the certain temperatures, at which
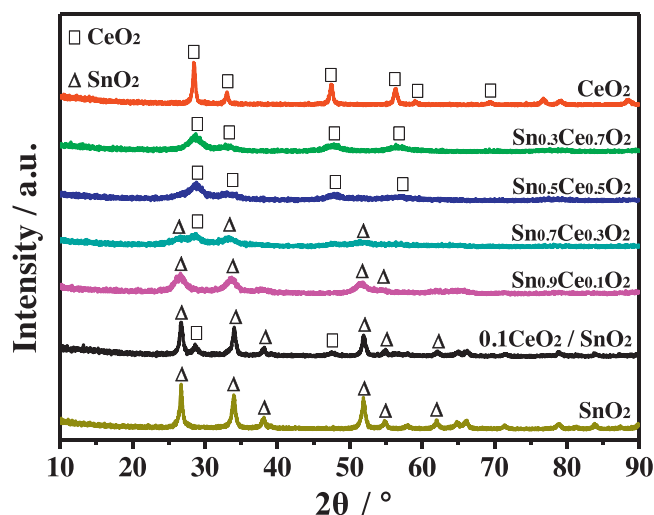
Fig. 1. XRD patterns of the catalysts.

the CH$_4$ conversion was less than 20%. Partial pressure dependencies of CH$_4$ and O$_2$ upon the reaction rates were measured by adjusting the corresponding gas concentrations, while keeping the total flow rate constant. In this work, the effect of water vapor to the methane combustion activity was also investigated by feeding water through a peristaltic pump. The reaction gas compositions were CH$_4$ (0.6–1.9 kPa), O$_2$ (0.9–9.6 kPa), and H$_2$O (0.9–9.6 kPa) in N$_2$.

The area-specific rate (r) were calculated as follows:

$$r = \frac{X_{[CH_4]} \times C_{[CH_4]}}{\left(W_{[Cat]} \times SSA\right)} \quad (3)$$

where $X_{[CH_4]}$ is the CH$_4$ conversion; $W_{[Cat]}$ is the weight of the loaded catalyst; $C_{[CH_4]}$ is the CH$_4$ molar flow in the feeding gas; and SSA is the specific surface area of the catalyst.

3. Results and discussion

3.1. Structural properties

Fig. 1 shows the XRD patterns of the catalysts, which can be roughly divided into two types: the Ce-rich catalysts (Sn$_{0.3}$Ce$_{0.7}$O$_2$ and Sn$_{0.5}$Ce$_{0.5}$O$_2$) and Sn-rich catalysts (Sn$_{0.9}$Ce$_{0.1}$O$_2$ and Sn$_{0.7}$Ce$_{0.3}$O$_2$). The diffraction peaks of all the Ce-rich catalysts could be indexed to the structure of CeO$_2$ (JCPDS no. 43-1002), and no SnO$_2$ phase was detected even for the Sn$_{0.5}$Ce$_{0.5}$O$_2$ catalyst. These results indicate that the Sn was dispersed on the CeO$_2$ surface and/or incorporated into the CeO$_2$ lattice. Regarding the amount of Sn in the Sn$_{0.3}$Ce$_{0.7}$O$_2$ and Sn$_{0.5}$Ce$_{0.5}$O$_2$ catalysts and the calcination temperature (650 °C) during the synthesis procedure, most of the Sn cations were probably incorporated into the CeO$_2$ lattice rather than dispersing on the CeO$_2$ surface. In Fig. 1,

the diffraction peaks of the Ce-rich catalysts broadened, and their lattice parameters slightly decreased with the increase of the Sn proportion (Table 1). Taking into the fact that the radius of the Sn cations (Sn^{2+}: 0.093 nm; Sn^{4+}: 0.071 nm) [29,30] was smaller than that of the Ce cations (Ce^{3+}: 0.110 nm; Ce^{4+}: 0.097 nm) [31,32], these findings demonstrate that the Sn cations were successfully incorporated into the CeO$_2$ lattice, leading to the shrinkage of the CeO$_2$ lattice. This deduction will be further confirmed in the following TEM and Raman characterizations.

Here, the SnO$_2$ phase was not observed on the Sn$_{0.5}$Ce$_{0.5}$O$_2$ catalyst, although it had the equal Sn and Ce contents. Considering that the SSA of the CeO$_2$ is larger than that of the SnO$_2$ (Table 1), it suggests that the thermodynamic stability of the CeO$_2$ phase is probably better than that of the SnO$_2$ phase. Consequently, the Sn$_{0.5}$Ce$_{0.5}$O$_2$ catalyst was in the form of the CeO$_2$ phase instead of the SnO$_2$ phase. Our XRD results are consistent with the previous study [26].

As for the Sn-rich catalysts, the XRD pattern of the Sn$_{0.9}$Ce$_{0.1}$O$_2$ catalyst was similar to that of the SnO$_2$ phase (JCPDS no. 41-1445), and no other phases was detected here. The lattice of the Sn$_{0.9}$Ce$_{0.1}$O$_2$ catalyst slightly expanded as compared with the SnO$_2$ catalyst (Table 1). Similarly, to the discussion with the Ce-rich catalysts, these results suggest that some Ce cations were substituted with the Sn cations, leading to the expanded lattice of the SnO$_2$. For the Sn$_{0.7}$Ce$_{0.3}$O$_2$ catalyst, both the SnO$_2$ and CeO$_2$ phases were detected from their weak and broad diffraction peaks. The SnO$_2$ lattice parameter of the Sn$_{0.7}$Ce$_{0.3}$O$_2$ catalyst (Table 1) was bigger than that of the Sn$_{0.9}$Ce$_{0.1}$O$_2$ catalyst, but the CeO$_2$ lattice parameter was similar to the pure CeO$_2$. These results indicate that the Ce element exists in both the SnO$_2$ lattice and the isolated CeO$_2$, which will be further identified in the following TEM characterization. As for the 0.1CeO$_2$/SnO$_2$ catalyst, both the CeO$_2$ and the SnO$_2$ phases were identified without any change of the lattice parameters, indicating that no Sn$_{1-x}$Ce$_x$O$_2$ composite was formed.

Table 1 gives the average crystallite size of the Sn-rich catalysts decreased as a function of the increased Ce loading, while the similar tendency was observed on the Ce-rich catalysts due to the Sn incorporation. Additionally, the surface areas of the Sn$_{1-x}$Ce$_x$O$_2$ catalysts, particularly the Sn$_{0.5}$Ce$_{0.5}$O$_2$ and Sn$_{0.7}$Ce$_{0.3}$O$_2$, was enlarged, as compared with the pure SnO$_2$ and CeO$_2$; while the surface area of the 0.1CeO$_2$/SnO$_2$ catalyst was similar to that of the pure SnO$_2$. Similar phenomenon was observed by the previous studies [15,26,33].

Fig. 2 shows the TEM images to observe the morphologies of the catalysts. The crystallite sizes of the Sn$_{1-x}$Ce$_x$O$_2$ catalysts (Fig. 2C$_1$, D$_1$, E$_1$, and F$_1$) were smaller than those of the pure SnO$_2$ and CeO$_2$ catalysts (Fig. 2A$_1$ and B$_1$), coinciding with the XRD results in Table 1. This might be the major reason why the Sn$_{1-x}$Ce$_x$O$_2$ catalysts achieved the larger SSAs.

In Fig. 2A$_2$, C$_2$, and D$_2$, the d-spacing values at around 0.335 nm for the Sn-rich catalysts were similar to that of the (1 1 0) plane of SnO$_2$, except that they slightly increased with the addition of the Ce dopant. This result coincided with the cell parameters listed in Table 1, further confirming formation of the SnO$_2$-based

Table 1
Phase composition, cell parameter, crystallite size, and specific surface area of the catalysts.

Catalyst	Cell parameter (nm)[a]	D (nm)[b]	SSA (m^2 g^{-1})
SnO$_2$	0.4722 (SnO$_2$)	16.4 (SnO$_2$)	28.4
Sn$_{0.9}$Ce$_{0.1}$O$_2$	0.4756 (SnO$_2$)	6.4 (SnO$_2$)	52.3
0.1CeO$_2$/SnO$_2$	0.4724 (SnO$_2$), 0.5412 (CeO$_2$)	15.7 (SnO$_2$), 9.0 (CeO$_2$)	25.6
Sn$_{0.7}$Ce$_{0.3}$O$_2$	0.4762 (SnO$_2$), 0.5412 (CeO$_2$)	4.4 (SnO$_2$), 6.2 (CeO$_2$)	76.1
Sn$_{0.5}$Ce$_{0.5}$O$_2$	0.5396 (CeO$_2$)	4.8 (CeO$_2$)	90.2
Sn$_{0.3}$Ce$_{0.7}$O$_2$	0.5401 (CeO$_2$)	5.4 (CeO$_2$)	53.1
CeO$_2$	0.5412 (CeO$_2$)	16.3 (CeO$_2$)	35.5

[a] Obtained from Fig. 1.
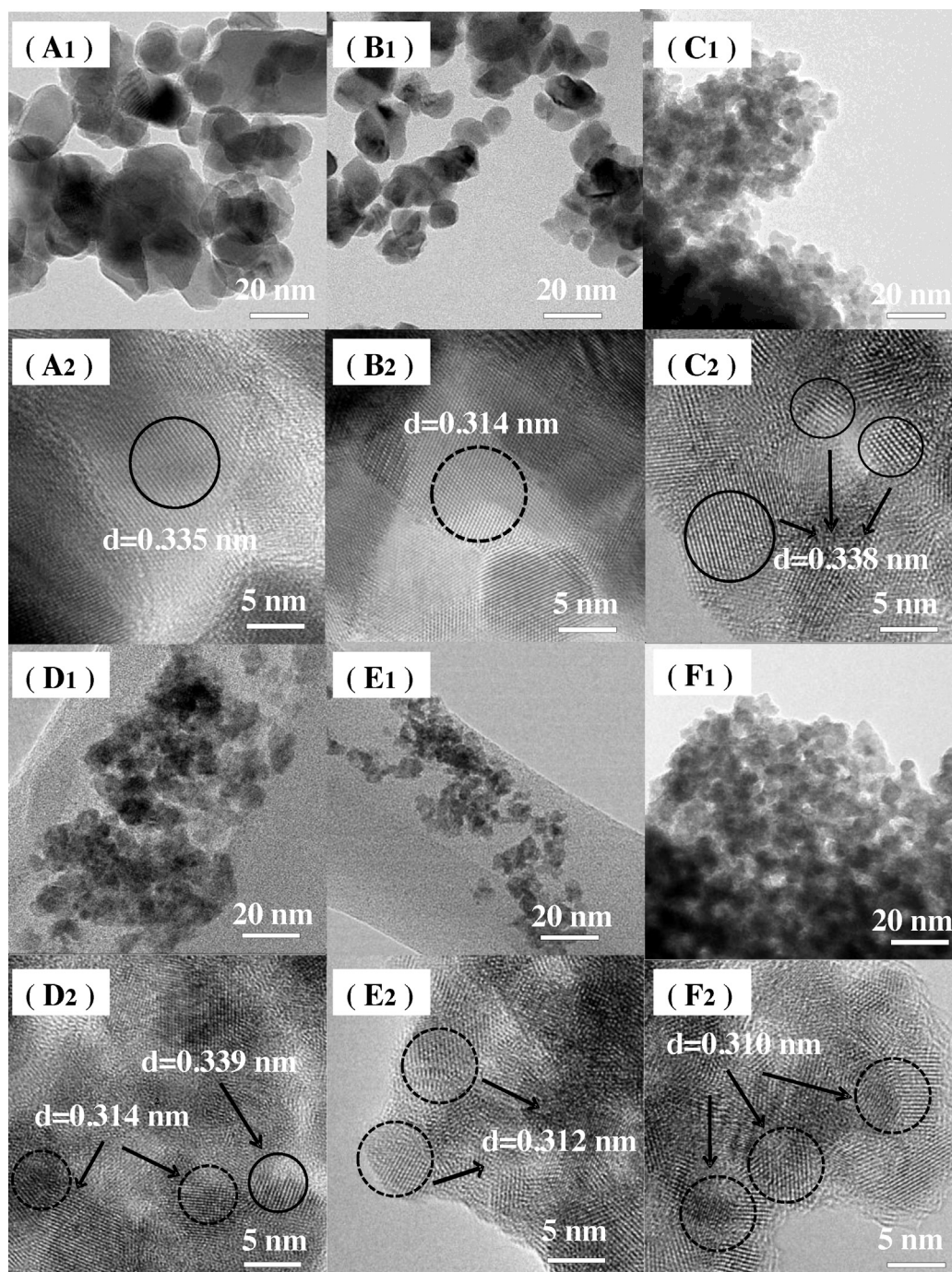[b] Calculated from the strongest diffraction peak by Scherrer equation in Fig. 1.

Fig. 2. TEM images of the catalysts: (A_1 and A_2) SnO_2; (B_1 and B_2) CeO_2; (C_1 and C_2) $Sn_{0.9}Ce_{0.1}O_2$; (D_1 and D_2) $Sn_{0.7}Ce_{0.3}O_2$; (E_1 and E_2) $Sn_{0.5}Ce_{0.5}O_2$; and (F_1 and F_2) $Sn_{0.3}Ce_{0.7}O_2$.

composites. Similarly, formation of the CeO_2-based composites for the Cd-rich catalysts was confirmed by comparison of the d-spacing values at around 0.314 nm in Fig. 2B_2, E_2, and F_2 with that of the (1 1 1) plane of CeO_2. Additionally, the d-spacing value of 0.314 nm in Fig. 2D_2 was comparable with that of the CeO_2 in Fig. 2B_2, indicating the presence of the isolated CeO_2 particles in the $Sn_{0.7}Ce_{0.3}O_2$ catalyst. It is in a good agreement with the XRD results, as well.

Fig. 3 shows two detectable Raman active modes of the SnO_2 catalyst: E_g (at around 460 cm^{-1}) and A_{1g} (at around 633 cm^{-1}) [34]. The A_{1g} peak is dominated by the lattice oxygen vibration, and its width is correlated with the crystallite size and the lattice oxygen defects [34,35]. The previous literature reported that decreasing the particle size of SnO_2 from more than 100–30 nm led to a widening

in FWHM about 5 cm^{-1} [34]. Our Raman results coincided with the XRD and TEM results that incorporating Ce into the Sn-rich catalysts decreased their crystallite sizes (Table 1). It is worth noting that the A_{1g} peak of the $Sn_{0.7}Ce_{0.3}O_2$ catalyst (Fig. 3e) widened and nearly vanished, as compared with the SnO_2 catalyst. However, the crystallite size of the $Sn_{0.7}Ce_{0.3}O_2$ catalyst only decreased about 10 nm. Thus, the variation of the bandwidth cannot be completely ascribed to the decrease of the particle size. The other possible reason is the presence of the bulk oxygen vacancies, which will lead to the distortion of the Sn—O bond [35].

The sharp peak at 469 cm^{-1} in Fig. 3a was ascribed to the F_{2g} vibration band of CeO_2 [36]. It continuously moved toward the lower Raman shifts and broadened for the 0.1CeO_2/SnO_2,
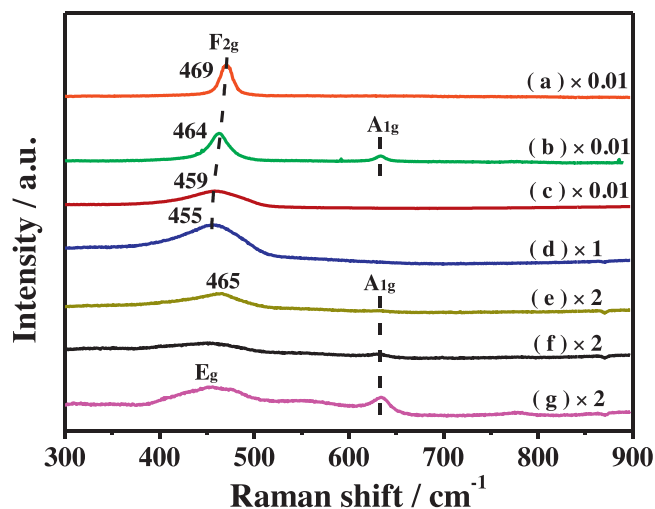
Fig. 3. Raman spectra of the catalysts: (a) CeO_2; (b) $0.1CeO_2/SnO_2$; (c) $Sn_{0.3}Ce_{0.7}O_2$; (d) $Sn_{0.5}Ce_{0.5}O_2$; (e) $Sn_{0.7}Ce_{0.3}O_2$; (f) $Sn_{0.9}Ce_{0.1}O_2$; and (g) SnO_2.

$Sn_{0.3}Ce_{0.7}O_2$ and $Sn_{0.5}Ce_{0.5}O_2$ catalysts (Fig. 3b–d). The Raman shift of this peak is strongly related to the decrease of the ceria crystallite size [36,37]. Additionally, the widening of the peak is sensitive to the symmetry of the crystal lattice [38]. The lower the symmetry of the crystal lattice is, the broader the peak is. Therefore, the lowered and broadened F_{2g} vibration bands of CeO_2 over the Ce-rich catalysts suggest that the incorporation of the Sn cations into the CeO_2 lattice inhibits the crystal growth and perturbs the structural symmetry of the Ce-rich catalysts. Herein, the F_{2g} band of the $Sn_{0.7}Ce_{0.3}O_2$ catalyst ($465\,cm^{-1}$) located at the similar Raman shift as that of the $0.1CeO_2/SnO_2$ ($464\,cm^{-1}$), although the former had a smaller ceria crystallite size (Table 1). This abnormal phenomenon might be due to the overlap of F_{2g} (CeO_2) and E_g (SnO_2) vibration bands.

The visible Raman spectroscopy employed in this work mainly supplies the bulk information of the catalysts [39]. Recent reports showed that the formation of the bulk oxygen vacancies on the CeO_2-based materials would produce two additional peaks at around 250 and $576\,cm^{-1}$ [40,41]. No related peak was observed in the Raman spectra of the Ce-rich catalysts in Fig. 3. Thus, the bulk oxygen vacancies might not be formed on these catalysts.

3.2. Performances for the catalytic combustion of methane

Fig. 4 shows the corresponding Arrhenius plots of the catalysts for the catalytic methane combustion. The associated activation energies (E_a) and pre-exponential factors (A) of the catalysts are
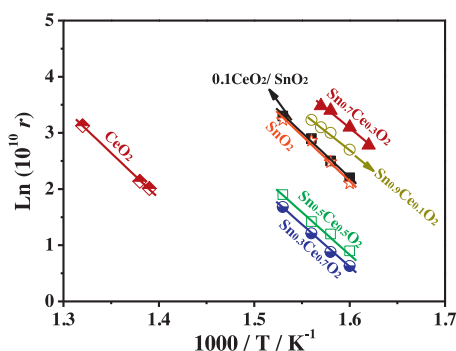

Fig. 4. Arrhenius plots of the catalysts upon the catalytic combustion of methane. Reaction conditions: $W_{[Cat]} = 0.2\,g$; feeding gas compositions = 0.6 kPa CH_4, 19 kPa O_2, N_2 balance; and flow rate = 235 mL min^{-1}.

Table 2
Activation energies (E_a) and pre-exponential factors (A) of the catalysts obtained from Arrhenius plots in Fig. 4.

Catalyst	E_a (kJ mol^{-1})	A ($10^{10} \times s^{-1}$)
SnO_2	129 ± 5	3.1
$Sn_{0.9}Ce_{0.1}O_2$	115 ± 4	2.3
$Sn_{0.7}Ce_{0.3}O_2$	109 ± 5	1.6
$Sn_{0.5}Ce_{0.5}O_2$	120 ± 4	0.5
$Sn_{0.3}Ce_{0.7}O_2$	123 ± 4	0.4

Reaction conditions: $W_{[Cat]} = 0.2\,g$; feeding gas compositions = 0.6 kPa CH_4, 19 kPa O_2, N_2 balance; and flow rate = 235 mL min^{-1}. The 90% confidence interval was reported and the maximal errors of E_a was ±5 kJ mol^{-1}.

calculated and listed in Table 2. Both the E_a and A values of the $Sn_{1-x}Ce_xO_2$ catalysts were lower compared with the pure SnO_2 catalyst. This phenomenon will be explained in the Section 3.5.

The area-specific rates (r) of the catalysts are calculated and compared with the literature values [20,42–45], as listed in Table 3. Clearly, the area-specific rate decreased in the sequence of $Sn_{0.7}Ce_{0.3}O_2 > Sn_{0.9}Ce_{0.1}O_2 > 0.1CeO_2/SnO_2 \approx SnO_2 > Sn_{0.5}Ce_{0.5}O_2 > Sn_{0.3}Ce_{0.7}O_2 > CeO_2$. The $0.1CeO_2/SnO_2$ catalyst exhibited the similar area-specific rate to the pure SnO_2, indicating that the CeO_2 dispersed on the SnO_2 surface had little impact on it. Therefore, the improved area-specific rate of the Sn-rich catalysts may be mainly due to the electron interaction between the Sn^{4+}/Sn^{2+} and Ce^{4+}/Ce^{3+} redox couples in the solid solution instead of the phase cooperation. Herein, the area-specific rates of the SnO_2 [20] and CeO_2 catalyst [45] are similar with the reported values, and the $Sn_{0.7}Ce_{0.3}O_2$ catalyst exhibited the comparable or even higher area-specific rate, as compared with the recently reported non-noble metal based catalysts [42–44]. Additionally, the function of the reaction temperature to the methane conversion is displayed in Fig. S2, and the $Sn_{0.7}Ce_{0.3}O_2$ catalyst shows the highest apparent activity.

3.3. Chemical states

X-ray absorption near edge structures (XANES) are frequently employed to probe average valences of metal cations. Fig. 5a shows the normalized XANES spectra (Sn K-edge) of the catalysts. They exhibited the similar absorption edge features, indicating that in all catalysts the tetra-valence of the Sn cations was the dominant oxidation state despite of the different Sn/Ce ratios [46].

Fig. 5b shows the normalized XANES spectra (Ce L$_3$-edge) of the catalysts and the reference sample $Ce(NO_3)_3 \cdot 6H_2O$. In Fig. 5b, the peak A is the characteristics of Ce^{4+}, while the low-energy peak B is assigned to Ce^{3+} [47]. This difference is an important judgment on distinguishing Ce^{3+} and Ce^{4+} compounds [47]. The CeO_2, $0.1CeO_2/SnO_2$, $Sn_{0.3}Ce_{0.7}O_2$, and $Sn_{0.5}Ce_{0.5}O_2$ catalysts had similar peak shapes, and thus, the Ce cations therein should be predominantly tetra-valent. Although the peak A was dominant in the $Sn_{0.7}Ce_{0.3}O_2$ catalyst, a shoulder peak B can also be observed, demonstrating the coexistence of Ce^{3+} and Ce^{4+}. The feature peak B of the $Sn_{0.9}Ce_{0.1}O_2$ catalyst became more evident, indicating the increased Ce^{3+}/Ce^{4+} ratio in bulk.

The XPS experiments are performed to further investigate the superficial chemical states and compositions of these catalysts. Fig. 6 presents the XPS spectra in the Sn 3d$_{5/2}$ region upon the $Sn_{1-x}Ce_xO_2$ catalysts. According to the NIST XPS database, the binding energy of SnO ranged from 485.6 to 487.0 eV and the binding energy of SnO_2 ranged from 486.0 to 487.1 eV [48]. Herein, the $Sn_{0.3}Ce_{0.7}O_2$ catalyst exhibited two shoulder peaks located at 486.0 and 486.9 eV, which could be assigned to Sn^{2+} and Sn^{4+}, respectively. With the decreased Ce incorporation, the two BE peaks gradually overlapped to a broad one, which shifted toward the
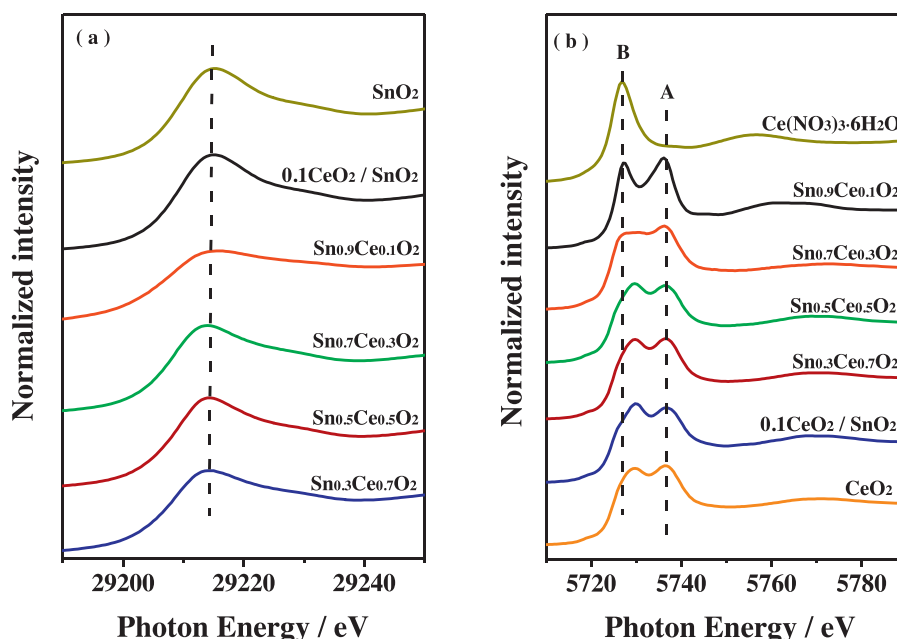
Fig. 5. XANES spectra of the catalysts: (a) Sn K-edge and (b) Ce L_3-edge.

higher BE. It indicates the qualitatively increased $Sn^{4+}/(Sn^{4+} + Sn^{2+})$ molar ratios (denoted as "Sn^{4+} ratio"). Table 4 gives the quantitative Sn^{4+} content by decomposing the XPS spectra. The Sn^{4+} ratio dropped from 96% (SnO_2) to 40% ($Sn_{0.3}Ce_{0.7}O_2$), associating with the decreased Sn content, while the superficial $Ce^{3+}/(Ce^{4+} + Ce^{3+})$ molar ratios (denoted as "Ce^{3+} ratio") increased with the increased Sn content, as indicated in Fig. S3. Additionally, in Fig. S4 and Table S1, the XPS results in the O 1s region clearly show that more surface lattice oxygen existed on the Sn-rich catalysts among the $Sn_{1-x}Ce_xO_2$ catalysts. Considering that the Sn-rich catalysts had the higher apparent catalytic activity in Fig. S2, as compared with

the Ce-rich ones, the XPS results in the O 1s region indicate that the surface lattice oxygen probably plays a key role for methane combustion.

For the principle of electric neutrality, the oxygen vacancies will be formed when the lower valent cations incorporate into the parent metal oxides [49]. The XANES and XPS results show that the Ce^{3+} cations existed not only on the surface but also in the bulk for the $Sn_{0.9}Ce_{0.1}O_2$ and $Sn_{0.7}Ce_{0.3}O_2$ catalysts. Consequently, the oxygen vacancies were generated, associating with the Ce^{3+} cations nearby. With respect to the $Sn_{0.3}Ce_{0.7}O_2$ and $Sn_{0.5}Ce_{0.5}O_2$ catalysts, the Sn^{2+} and Ce^{3+} cations mainly existed on the surface instead of

Table 3
Area-specific rates (r) of the catalysts upon the catalytic combustion of methane.

Catalyst	r ($10^{-9} \times mol\,m^{-2}\,s^{-1}$)	Feeding gas compositions	Ref.
SnO_2[a]	1.2	0.5% CH_4 and 20% O_2 in N_2	This work
$0.1CeO_2/SnO_2$[a]	1.3	0.5% CH_4 and 20% O_2 in N_2	This work
$Sn_{0.9}Ce_{0.1}O_2$[a]	1.9	0.5% CH_4 and 20% O_2 in N_2	This work
$Sn_{0.7}Ce_{0.3}O_2$[a]	2.9	0.5% CH_4 and 20% O_2 in N_2	This work
$Sn_{0.5}Ce_{0.5}O_2$[a]	0.4	0.5% CH_4 and 20% O_2 in N_2	This work
$Sn_{0.3}Ce_{0.7}O_2$[a]	0.3	0.5% CH_4 and 20% O_2 in N_2	This work
CeO_2[a]	0.06	0.5% CH_4 and 20% O_2 in N_2	This work
CeO_2[b]	1.8	0.5% CH_4 and 20% O_2 in N_2	This work
SnO_2[a]	1.0	1.5% CH_4 and 18% O_2 in N_2	[20]
$Co_3O_4/SBA-15$[a]	1.4	0.25% CH_4 and 8% O_2 in N_2	[42]
$La_{0.6}Sr_{0.4}MnO_3$[a]	2.0	1% CH_4 and 8% O_2 in N_2	[43]
$Cu_{(10at\%)}ZnAlO$[a]	0.7	1% CH_4 and 21% O_2 in N_2	[44]
CeO_2[b]	2.0	10% CH_4 and 21% O_2 in He	[45]

[a] The area-specific rates measured at 360 °C.
[b] The area-specific rates measured at 560 °C.

Table 4
Molar ratio of the metal cations on the surface of the catalysts determined by XPS.

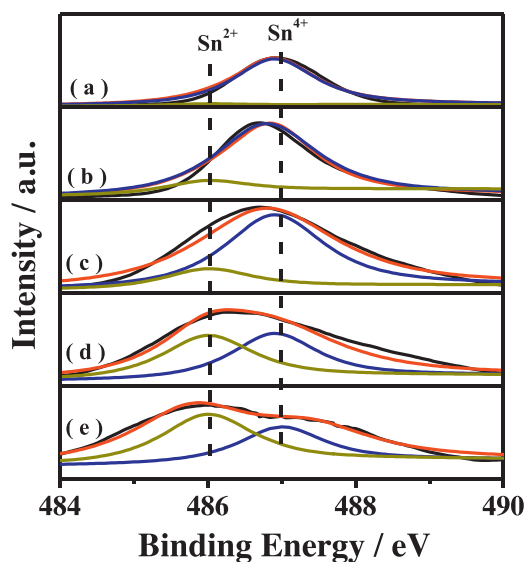| Catalyst	Sn/Sn + Ce (%)	$Sn^{4+}/Sn^{4+} + Sn^{2+}$ (%)	$Ce^{3+}/Ce^{4+} + Ce^{3+}$ (%)	$Sn^{4+}/Sn + Ce$ (%)	$Ce^{3+}/Sn + Ce$ (%)
SnO_2	100	96	/	96	/
$Sn_{0.9}Ce_{0.1}O_2$	82	88	28	72	5
$Sn_{0.7}Ce_{0.3}O_2$	66	80	24	53	8
$Sn_{0.5}Ce_{0.5}O_2$	36	51	17	18	11
$Sn_{0.3}Ce_{0.7}O_2$	26	40	18	10	13
CeO_2	/	/	14	/	14

Fig. 6. XPS spectra in the Sn $3d_{5/2}$ region: (a) SnO_2; (b) $Sn_{0.9}Ce_{0.1}O_2$; (c) $Sn_{0.7}Ce_{0.3}O_2$; (d) $Sn_{0.5}Ce_{0.5}O_2$; and (e) $Sn_{0.3}Ce_{0.7}O_2$.

the bulk; accordingly, the oxygen vacancies dominantly located on the surface of these Ce-rich catalysts.

3.4. Redox behaviors of the catalysts

3.4.1. O_2-TPD and H_2-TPR measurements

The O_2-TPD measurement is an effective method to characterize the nature of the oxygen vacancies and surface oxygen species. Fig. 7 shows the O_2-TPD profiles of the $Sn_{1-x}Ce_xO_2$ catalysts, and two distinguishable peaks were observed. Generally, the oxygen desorption peak at lower temperatures, denoted as peak α, is related to the oxygen bonded on the oxygen vacancies, i.e., the so-called adsorbed oxygen species [50]; nevertheless, the peak at higher temperatures, denoted as peak β, is assigned to the desorption of the surface lattice oxygen [50]. With the aid of oxygen vacancies, the migration of the lattice oxygen from bulk to surface also occurs [51].

For the pure CeO_2 and SnO_2 catalysts, the intensity of the peak α is negligible. In Fig. 7, the desorption temperatures of the peak α decreased in the order of
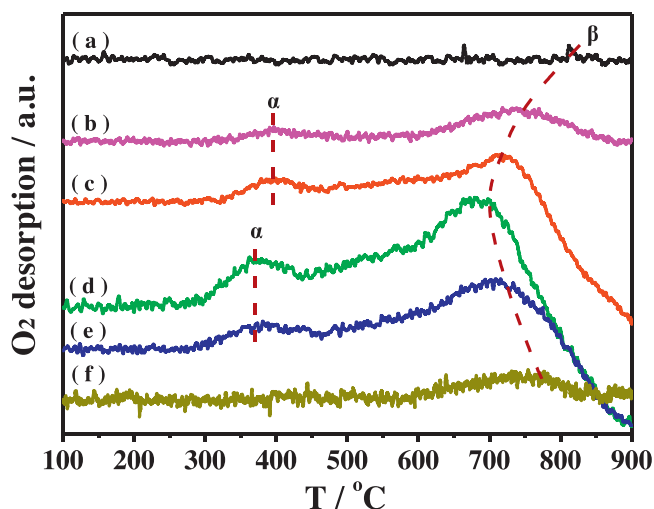

Fig. 7. O_2-TPD profiles of the catalysts: (a) CeO_2; (b) $Sn_{0.3}Ce_{0.7}O_2$; (c) $Sn_{0.5}Ce_{0.5}O_2$; (d) $Sn_{0.7}Ce_{0.3}O_2$; (e) $Sn_{0.9}Ce_{0.1}O_2$; and (f) SnO_2.

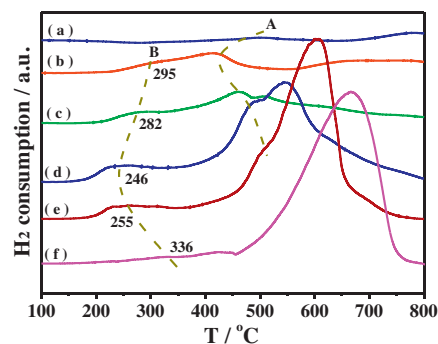**Fig. 8.** H_2-TPR profiles of the catalysts: (a) CeO_2; (b) $Sn_{0.3}Ce_{0.7}O_2$; (c) $Sn_{0.5}Ce_{0.5}O_2$; (d) $Sn_{0.7}Ce_{0.3}O_2$; (e) $Sn_{0.9}Ce_{0.1}O_2$; and (f) SnO_2.

$Sn_{0.3}Ce_{0.7}O_2 \approx Sn_{0.5}Ce_{0.5}O_2 > Sn_{0.7}Ce_{0.3}O_2 \approx Sn_{0.9}Ce_{0.1}O_2$. The lower desorption temperatures for the $Sn_{0.7}Ce_{0.3}O_2$ and $Sn_{0.9}Ce_{0.1}O_2$ catalysts were induced by the weaker bonding energy between the adsorbed oxygen and oxygen vacancies, which would lead to the better oxygen mobility. Moreover, the oxygen transfer in the $Sn_{0.5}Ce_{0.5}O_2$ and $Sn_{0.3}Ce_{0.7}O_2$ catalysts was mainly through the surface oxygen vacancies, as indicated by the Raman, XANES, and XPS results. Nevertheless, for the $Sn_{0.9}Ce_{0.1}O_2$ and $Sn_{0.7}Ce_{0.3}O_2$ catalysts, the coexistence of the surface and bulk oxygen vacancies could further accelerate the oxygen transfer [50].

No β oxygen was observed in the case of the pure CeO_2. The desorption temperatures of the peak β decreased in the order of $SnO_2 > Sn_{0.3}Ce_{0.7}O_2 > Sn_{0.5}Ce_{0.5}O_2 > nSn_{0.9}Ce_{0.1}O_2 > Sn_{0.7}Ce_{0.3}O_2$. Additionally, the desorption areas were enlarged with formation of the SnO_2–CeO_2 solid solution, especially for the Sn-rich catalysts, as shown in Fig. 7. Thus, we can draw a conclusion that formation of the SnO_2–CeO_2 composites not only activates the surface oxygen, including both the surface adsorbed oxygen and surface lattice oxygen, but also enlarges their quantities, especially for the Sn-rich catalysts.

Fig. 8 displays the H_2-TPR profiles of the $Sn_{1-x}Ce_xO_2$ catalysts. The H_2-TPR profile of the pure CeO_2 shows two broad and weak reduction peaks. The peak from 450 to 600 °C was ascribed to the reduction of the surface Ce^{4+}, and the peak above 600 °C was assigned to the reduction of the bulk CeO_2 [15]. In the H_2-TPR profile of the pure SnO_2, the shoulder reduction peaks were clearly observed. Generally, Sn^{4+} can only be reduced to Sn^{2+} below 500 °C [15,26]. In Fig. 8f, the shoulder reduction peak ranging from 250 to 500 °C was attributed to the reduction of the surface Sn^{4+} to Sn^{2+}, while the reduction peak at higher temperatures was assigned to the reduction of the bulk SnO_2, as well as the surface Sn^{2+} to Sn^0. By comparison of the H_2-TPR profiles of the pure CeO_2 and SnO_2, it is obvious that the reducibility of the Sn^{4+} cations was much higher than that of the Ce^{4+} cations.

Upon the $Sn_{1-x}Ce_xO_2$ catalysts, the peak A and B in Fig. 8b–e could be attributed to the reduction of the surface Ce^{4+} and Sn^{4+}, respectively. To investigate the reducibility and quantity of the surface Ce^{4+} and Sn^{4+} cations, we fitted the H_2-TPR profiles in Fig. S6. The reduction peak A upon the $Sn_{1-x}Ce_xO_2$ catalysts shifted toward the lower temperatures compared with the pure CeO_2, especially for the Ce-rich catalysts. Moreover, the amount of the surface Ce^{4+} over the $Sn_{1-x}Ce_xO_2$ catalysts (Table S2) was much larger than that of the pure CeO_2. These results indicate that both the reducibility and quantity of the surface Ce^{4+} cations were enhanced after the formation of the SnO_2–CeO_2 solid solutions. The previous study reported that doping with Cu into the CeO_2 lattice was beneficial to the redox equilibrium of $Cu^{2+} + Ce^{3+} \leftrightarrow Cu^+ + Ce^{4+}$, and the reducibility of Cu^{2+} and Ce^{4+} could be simultaneously pro-

Table 5
Amounts of the surface Sn^{4+} cations and TOF values of the catalysts.

Catalyst	Area-specific surface Sn^{4+} ($\mu mol\ m^{-2}$)[a]	TOF ($10^{-5} \times s^{-1}$)[b]
SnO_2	36	3.1
$Sn_{0.9}Ce_{0.1}O_2$	22	7.7
$Sn_{0.7}Ce_{0.3}O_2$	18	15.6
$Sn_{0.5}Ce_{0.5}O_2$	7	4.5
$Sn_{0.3}Ce_{0.7}O_2$	6	4.1

[a] Calculated from the peak fit results in Fig. S6.
[b] Reaction conditions: $W_{[Cat]} = 0.2$ g; feeding gas compositions = 0.6 kPa CH_4, 19 kPa O_2, N_2 balance; flow rate = 235 mL min^{-1}; and $T = 360\,^\circ C$.

moted [35]. Thus, as compared with the pure CeO_2, the enhanced reducibility of the surface Ce^{4+} on the $Sn_{1-x}Ce_xO_2$ catalysts was due to the existence of Sn^{4+}. According to the equilibrium of $Sn^{4+} + 2Ce^{3+} \leftrightarrow Sn^{2+} + 2Ce^{4+}$, the reducibility of the surface Ce^{4+} could be further enhanced by increasing the surface Ce^{4+} content, which increased with the addition of Ce to the $Sn_{1-x}Ce_xO_2$ catalysts, as determined by XPS in Table 4.

In Fig. 8, the reduction temperature of the surface Sn^{4+} on the SnO_2 is higher than that on the $Sn_{1-x}Ce_xO_2$ catalysts (peak B). Similarly, to the discussion on the surface Ce^{4+}, the electron interaction through the redox equilibrium of $Sn^{4+} + 2Ce^{3+} \leftrightarrow Sn^{2+} + 2Ce^{4+}$ could enhance the reducibility of the surface Sn^{4+} on the $Sn_{1-x}Ce_xO_2$ catalysts. In Fig. 8b–e, as compared with the peak A, the reduction temperatures of the peak B lowered more than $100\,^\circ C$, indicating the much higher reducibility of the surface Sn^{4+}, which was in the order of $Sn_{0.3}Ce_{0.7}O_2 < Sn_{0.5}Ce_{0.5}O_2 < Sn_{0.9}Ce_{0.1}O_2 < Sn_{0.7}Ce_{0.3}O_2$, than that of the surface Ce^{4+}. Strangely, the reduction temperature of the peak B for the $Sn_{0.7}Ce_{0.3}O_2$ catalyst was lower than that for the $Sn_{0.9}Ce_{0.1}O_2$, in spite of the latter's higher surface Sn^{4+} content (Table 4). The possible explanation is that the smaller crystallite size and lower structure symmetry (XRD, Raman, and EXAFS results in Table 1, Figs. 3 and S5) can further enhance the reducibility of the surface Sn^{4+} cations on the $Sn_{0.7}Ce_{0.3}O_2$ catalyst, as compared with the $Sn_{0.9}Ce_{0.1}O_2$.

Herein, the reducibility sequence of the surface Sn^{4+} cations coincided with the area-specific rate sequence (Table 3) upon the $Sn_{1-x}Ce_xO_2$ catalysts. Probably, the surface Sn^{4+} cations on the $Sn_{1-x}Ce_xO_2$ catalysts are the active sites for methane combustion. However, this assumption cannot explain the contradictory sequence concerning the reducibility of the surface Sn^{4+} and the catalytic behavior with the SnO_2 and Ce-rich catalysts. Table 5 gives the quantity of the surface Sn^{4+} cations, basing on the decomposing results from Fig. S6. Apparently, the quantity per surface area of the surface Sn^{4+} on the SnO_2 is around 5–6 times larger than that of the Ce-rich catalysts. This will induce the higher area-specific rate of the SnO_2 than those of the Ce-rich catalysts. Additionally, the excellent reversibility of the surface $Sn^{4+} \leftrightarrow Sn^{2+}$ was evidenced by alternatively switching the reducing and oxidizing atmospheres upon the $Sn_{0.7}Ce_{0.3}O_2$ catalyst, as shown in Fig. S7.

3.4.2. CH_4-TPSR measurements

To further investigate the catalytic behavior of the catalysts in the presence of the CH_4 reactant, the CH_4-TPSR experiments were preformed, as shown in Fig. 9. During these tests, no CO signal was detected, indicating no partial oxidation of methane occurred [52–54]. The profiles of the CeO_2 and SnO_2 catalysts, which were pretreated in the O_2/N_2 flow at $450\,^\circ C$, showed a weak and broad peak ranging from 400 to $900\,^\circ C$ (Fig. 9a and b). Nevertheless, the $Sn_{0.7}Ce_{0.3}O_2$ catalyst with the same pretreatment exhibited two peaks (Fig. 9c). The H_2-TPR results show that the surface Sn^{4+} cations was more active than the surface Ce^{4+} cations. Thus, the peak locating at the lower temperatures, denoted as X, could be assigned to the reduction of the surface Sn^{4+}; while the peak locat-
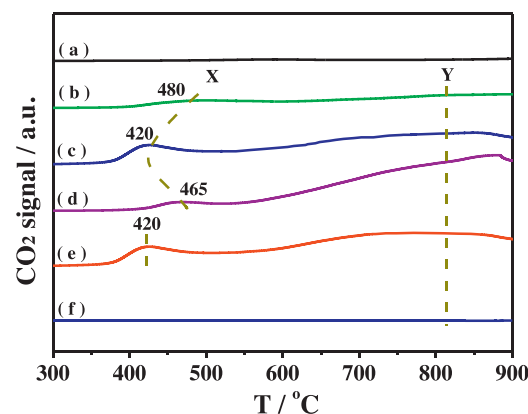

Fig. 9. CH_4-TPSR profiles of the catalysts: (a) CeO_2 pretreated in the O_2/N_2 flow at $450\,^\circ C$; (b) SnO_2 pretreated in the O_2/N_2 flow at $450\,^\circ C$; (c) $Sn_{0.7}Ce_{0.3}O_2$ pretreated in the O_2/N_2 flow at $450\,^\circ C$; (d) $Sn_{0.3}Ce_{0.7}O_2$ pretreated in the O_2/N_2 flow at $450\,^\circ C$; (e) $Sn_{0.7}Ce_{0.3}O_2$ pretreated in the N_2 flow at $450\,^\circ C$; and (f) $Sn_{0.7}Ce_{0.3}O_2$ pretreated in the N_2 flow at $700\,^\circ C$.

ing at the higher temperatures, denoted as Y, could be assigned to the reduction of the surface Ce^{4+} cations and probably a part of the bulk Sn^{4+} cations, as well. Additionally, Fig. 9c and d shows that the area of the peak X of the $Sn_{0.7}Ce_{0.3}O_2$ catalyst was more pronounced than that of the $Sn_{0.3}Ce_{0.7}O_2$, and the former's reduction temperature lowered about $45\,^\circ C$ than the latter's, as well. It indicates the larger quantity and higher reducibility of the surface Sn^{4+} cations on the $Sn_{0.7}Ce_{0.3}O_2$ catalyst, which are in a good agreement with the H_2-TPR results in Fig. 8 and Table 5.

To distinguish the nature of the surface oxygen species, we removed the surface adsorbed oxygen from the $Sn_{0.7}Ce_{0.3}O_2$ catalyst, as indicated in Fig. S8, by the pretreatment in the N_2 flow at $450\,^\circ C$ for 0.5 h. Its CH_4 reduction behavior (Fig. 9e) was similar to that of the surface adsorbed oxygen remained catalyst (Fig. 9c). If we further removed the surface lattice oxygen by heating in the N_2 flow at $700\,^\circ C$ for 0.5 h, no evident CH_4-TPSR peak was observed in Fig. 9f. These results provided the direct evidence that the surface lattice oxygen, instead of the surface adsorbed oxygen, was the key species involved in the methane combustion. These results are consistent with the previous studies [52–54].

3.5. Kinetics measurements

3.5.1. Reaction orders for CH_4, O_2 and H_2O

To fully understand the reaction mechanism, we investigated the reaction orders for CH_4, O_2, and H_2O over the SnO_2, $Sn_{0.7}Ce_{0.3}O_2$, and $Sn_{0.3}Ce_{0.7}O_2$ catalysts. The reaction order for CH_4 over the SnO_2 and $Sn_{1-x}Ce_xO_2$ ($x = 0.3$ and 0.7) catalysts was 0.8 and 1.0, respectively, as shown in Fig. 10a. These values were comparable to the data reported over the $Ce_{1-x}La_xO_2$ catalysts [45]. It suggests that the reaction rate strongly depends on the CH_4 partial pressure.

The reaction order for the gaseous O_2 over the $Sn_{0.7}Ce_{0.3}O_2$ catalysts was zero in Fig. 10b. It indicates that the reaction rates on the replenishment of the consumed active oxygen species, i.e., surface lattice oxygen, are fast enough so that the concentration of the gaseous oxygen has little influence on it. The similar result was observed on the SnO_2 catalyst. Nevertheless, the reaction order for O_2 over the $Sn_{0.3}Ce_{0.7}O_2$ catalyst was slightly higher than zero, i.e., 0.1. Wilkes et al. reported that the reaction order for O_2 over the $Ce_{1-x}La_xO_2$ catalysts increased from 0.2 to 0.4 when the phase composition changed from CeO_2 to La_2O_3 [45]. Here, the different phases of the $Sn_{0.3}Ce_{0.7}O_2$ catalyst (CeO_2 phase) and the $Sn_{0.7}Ce_{0.3}O_2$ and SnO_2 catalysts (SnO_2 phase) might be the major reason for the slightly increased reaction order for O_2 over the
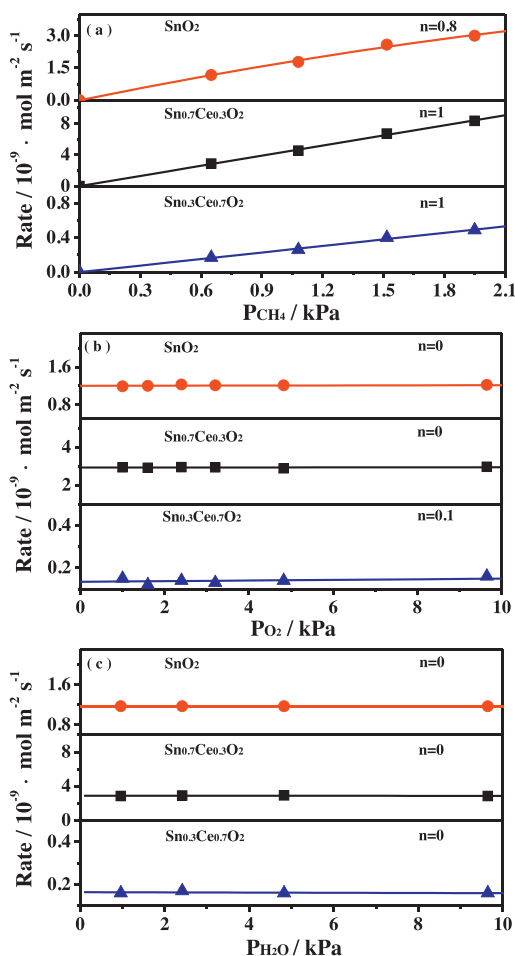
Fig. 10. Dependence of reaction rates on the partial pressure of the gas compositions upon the catalytic combustion of methane: (a) 0.6–1.9 kPa CH_4, 19 kPa O_2, 0 kPa H_2O; (b) 0.6 kPa CH_4, 0.9–9.6 kPa O_2, 0 kPa H_2O; (c) 0.6 kPa CH_4, 19 kPa O_2, and 0.9–9.6 kPa H_2O. Reaction conditions: $W_{[Cat]}$ = 0.2 g; flow rate = 235 mL min^{-1}; and T = 360 °C.

$Sn_{0.3}Ce_{0.7}O_2$ catalyst. Moreover, the combined Raman, XANES, XPS, and O_2-TPD results showed that the Sn-rich catalysts exhibited the better oxygen mobility than the Ce-rich catalysts. Thus, over the $Sn_{0.3}Ce_{0.7}O_2$ catalyst, the other possibility concerning the slightly increased reaction order for O_2 might be due to the relatively slower replenishment rate of the consumed surface lattice oxygen.

In summary, the methane combustion reaction presented the zero reaction order for O_2 and the pseudo-first-order apparent dependence on the CH_4 partial pressure over the SnO_2 and $Sn_{0.7}Ce_{0.3}O_2$ catalysts. It follows the typical Mars–van Krevelen model [55] over the Sn-rich catalysts. This strongly supports our conclusion made in the CH_4-TPSR discussion in Fig. 9 that the surface lattice oxygen species plays the import role for methane activation. These findings also suggest that the rate determining step should be the dissociation of CH_4 [55]. Considering 0.1 of the reaction order for O_2 over the $Sn_{0.3}Ce_{0.7}O_2$ catalyst, over the Ce-rich catalysts other reaction mechanisms might also be obeyed besides the Mars–van Krevelen model.

The effect of H_2O on the total oxidation of methane over the non-noble metal catalysts is complicated. H_2O can promote the oxidation of methane over the ceria–zirconia [56] and cobalt–manganese catalysts [57], but inhibit the methane combustion over the $La_{1-x}Sr_xFeO_3$ catalysts [58]. Our work shows that H_2O little influenced this reaction, and the reaction order for H_2O was about 0, as presented in Fig. 10c. Moreover, in Figs. S9 and S10, the hydrothermal aged catalysts displayed the similar activity to
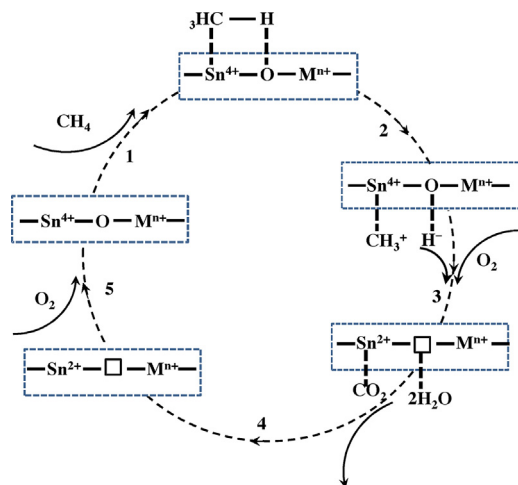
the fresh ones. These results indicate that the SnO_2-based catalysts display the high water resistance.

3.5.2. Discussion on the active sites

Herein, the activation energy (E_a) and pre-exponential factor (A) were analyzed in depth to further clarify the influencing factors on the catalytic performance. As listed in Table 2, the E_a values of the Sn-rich catalysts were lower than that of the SnO_2, and the $Sn_{0.7}Ce_{0.3}O_2$ catalyst had the lowest E_a value. Interestingly, the E_a values decreased following the lowered reduction temperatures of the surface Sn^{4+} in Fig. 8. It confirms that upon the Sn-rich catalysts E_a is directly linked to the reducibility of the surface Sn^{4+} cations, and the surface Sn^{4+} cations are active sites for methane combustion.

To further verify the above suggestion, the turnover frequency (TOF) via the surface Sn^{4+} is calculated and listed in Table 5:

$$TOF = \frac{r}{\text{the area} - \text{specific quantity of the surface } Sn^{4+}} \quad (4)$$

Apparently, formation of the $Sn_{1-x}Ce_xO_2$ solid solution activated the surface Sn^{4+} cations, and resulted in the high TOF values. Upon the Sn-rich catalysts, the increasing trend of the TOF values well coincided with that of the reducibility of the surface Sn^{4+} cations, as well as the decreasing trend of the E_a values. Among these catalysts, the $Sn_{0.7}Ce_{0.3}O_2$ exhibited the highest area-specific rate, and its TOF value was around five times higher than that of the SnO_2 catalyst.

The pre-exponential factors (A) is generally related to the quantity of the active sites [59]. Herein, the pre-exponential factor might be mainly influenced by the area-specific quantity of the surface Sn^{4+} determined by H_2-TPR in Table 5. As compared with the SnO_2, only a little difference in E_a was observed for the Ce-rich catalysts, but the A values of the Ce-rich catalysts were much smaller (Table 2). Consequently, the SnO_2 catalyst exhibited the higher area-specific rate than the Ce-rich catalysts. Nevertheless, for the Sn-rich catalysts, the relatively bigger difference in E_a became the major factor, instead of A, to determine the area-specific rates, which follows $SnO_2 < Sn_{0.9}Ce_{0.1}O_2 < Sn_{0.7}Ce_{0.3}O_2$.

3.6. Mechanistic suggestions

After analyzing the above discussed characterizations, we understand the improvement effect of the Ce doping for the catalytic combustion of methane over the SnO_2-based catalyst. Herein, the possible reaction pathways over the Sn-rich catalysts, which were in the SnO_2 phase, are proposed in Fig. 11.

Fig. 11. Possible methane oxidation pathways over the Sn-rich catalysts.

Four equivalent C—H bonds of CH_4 define a symmetrical tetrahedron. Considering that the reaction temperature was above 350 °C in this work, the CH_4 adsorption is neglectable at such high temperatures [60]. At the first stage, CH_4 attacks the acid–base pair (Sn^{4+}—O—M^{n+}, M^{n+}=Sn^{4+}, Sn^{2+}, Ce^{4+}, or Ce^{3+}) of the catalysts, leading to the structural distortion of CH_4.

At the second stage, CH_4 is dissociated into intermediate species, probably CH_3^+ and OH^- [45]. As we discussed above, the surface Sn^{4+} cations are active sites for methane combustion, and the reaction rate is nearly proportional to the partial pressure of CH_4. Thus, the dissociation of the C—H bond is the rate determining step during the methane combustion process.

At the third stage, the intermediate species (CH_3^+ and OH^-) are much more active than CH_4, and can be readily oxidized to CO_2 and H_2O by any available surface oxygen species therein; meanwhile, the surface Sn^{4+} cations are reduced to Sn^{2+}.

Thereafter, the surface Sn cation's neighboring surface lattice oxygen species are consumed with the releasing of CO_2 and H_2O. In many cases, the desorption of H_2O at the fourth stage is comparatively slow, consequently inhibiting the overall reaction rate of the reaction. In this work, the reaction order for H_2O was zero as indicated in the kinetics tests (Fig. 10c). It suggests that the adsorbability of H_2O over these SnO_2-based catalyst is very weak, and the produced H_2O during the methane combustion is easily desorbed to regenerate the active sites. Accordingly, the overall reaction rate is not controlled by these steps.

At the last stage (stage 5), the consumed surface lattice oxygen will be regenerated mainly from the gaseous O_2, as well as the migration of the bulk lattice oxygen. Because the reaction rate is independent of the gaseous oxygen, these surface lattice oxygen compensating steps are fast enough, and have little impact on the whole reaction.

4. Conclusions

Herein, the $Sn_{1-x}Ce_xO_2$ solid solution catalysts were synthesized by the co-precipitation method and evaluated by the catalytic combustion of methane. Our results show that doping with Ce into the SnO_2 catalyst enlarged the SSA, promoted the formation of the oxygen vacancies, enhanced the reducibility of the surface Sn^{4+} cations and activated the surface oxygen species, including the surface adsorbed oxygen and the surface lattice oxygen. The area-specific rates of these catalysts displayed the volcano-type tendency with the addition of Ce. The $Sn_{0.7}Ce_{0.3}O_2$ catalyst presented the highest catalytic performance with about five times higher TOF value than the SnO_2.

The surface Sn^{4+} cations are active sites for methane combustion, and the surface lattice oxygen also plays the essential role in this process. The Raman, XANES, and XPS results show the coexistence of the surface and bulk oxygen vacancies on the Sn-rich catalysts (SnO_2 phase); while for the Ce-rich catalysts (CeO_2 phase), the oxygen vacancies mainly existed on the surface. Thus, the former catalysts exhibit the better oxygen mobility than the latter ones. Experimentally, we observed that the reaction rate over the Sn-rich catalysts was independent of the concentration of the gaseous oxygen. Nevertheless, the concentration of the gaseous oxygen had a little impact on the reaction rate upon the Ce-rich catalysts. Additionally, water vapor had little impact on the reaction rates.

Our findings indicate that the Mars–van Krevelen model is preferred over the Sn-rich catalysts upon the catalytic combustion of methane. The dissociation of the C—H bond is the rate determining step because the activation energy (E_a) and TOF was strongly related to the reducibility of the surface Sn^{4+} cations for the Sn-rich catalysts. The area-specific quantity of the surface Sn^{4+} on

the catalyst directly linked to the pre-exponential factor (A). Thus, the $Sn_{0.7}Ce_{0.3}O_2$ catalyst exhibited the highest area-specific rate because of its lowest E_a and relatively bigger A. These Ce doped SnO_2 materials will be one of the potential catalysts with the high water-resistance ability for the catalytic combustion of methane.

Appendix A. Supplementary data

Supplementary data associated with this article can be found, in the online version, at http://dx.doi.org/10.1016/j.apcatb.015.04.042.

References

[1] H. Brix, B.K. Sorrell, B. Lorenzen, Aquat. Bot. 69 (2001) 313–324.
[2] D.L. Trimm, C.W. Lam, Chem. Eng. Sci. 35 (1980) 1405–1413.
[3] F. Yin, S. Ji, P. Wu, F. Zhao, C. Li, J. Catal. 257 (2008) 108–116.
[4] W.R. Schwartz, D. Ciuparu, L.D. Pfefferle, J. Phys. Chem. C 116 (2012) 8587–8593.
[5] X. Liu, J. Liu, F. Geng, Z. Li, P. Li, W. Gong, Front. Chem. Sci. Eng. 6 (2012) 34–37.
[6] R.S. Monteiro, D.Y. Zemlyanov, J.M. Storey, F.H. Ribeiro, J. Catal. 199 (2001) 291–301.
[7] G. Zhu, J. Han, D.Y. Zemlyanov, F.H. Riberio, J. Am. Chem. Soc. 126 (2004) 9896–9897.
[8] J. Chen, W. Shi, X. Zhang, H. Arandiyan, D. Li, J. Li, Environ. Sci. Technol. 45 (2011) 8491–8497.
[9] W. Shan, M. Luo, P. Ying, W. Shen, C. Li, Appl. Catal. A 246 (2003) 1–9.
[10] J. Xu, P. Li, X. Song, C. He, J. Yu, Y.F. Han, J. Phys. Chem. Lett. 1 (2010) 1648–1654.
[11] Y. Zhang, Z. Qin, G. Wang, H. Zhu, M. Dong, S. Li, Z. Wu, Z. Li, Z. Wu, J. Zhang, T. Hu, W. Fan, J. Wang, Appl. Catal. B 129 (2013) 172–181.
[12] Y. Wang, J. Ren, Y. Wang, F. Zhang, X. Liu, Y. Guo, G. Lu, J. Phys. Chem. C 112 (2008) 15293–15298.
[13] X. Wei, P. Hug, R. Figi, M. Trottmann, A. Weidenkaff, D. Ferri, Appl. Catal. B 94 (2010) 27–37.
[14] S. Wang, G. Xue, J. Liang, Y. Yuan, X. Zhang, Catal. Commun. 45 (2014) 39–43.
[15] X. Yao, X. Xiong, W. Zou, L. Zhang, S. Wu, X. Dong, F. Gao, Y. Deng, C. Tang, Z. Chen, L. Dong, Y. Chen, Appl. Catal. B 144 (2014) 152–165.
[16] C. Kilic, A. Zunger, Phys. Rev. Lett. 88 (2002) 9.
[17] L. Wei, J. Li, X. Tang, Catal. Lett. 127 (2009) 107–112.
[18] X. Han, X. Xu, W. Liu, X. Wang, R. Zhang, Solid State Sci. 20 (2013) 103–109.
[19] Y. Sun, F. Lei, S. Gao, J. Pan, J. Zhou, Y. Xie, Angew. Chem. Int. Ed. 125 (2013) 10763–10766.
[20] X. Wang, Y.C. Xie, Appl. Catal. B 35 (2001) 85–94.
[21] X. Wang, Y.C. Xie, Catal. Lett. 75 (2001) 73–80.
[22] G. Dutta, U.V. Waghmare, T. Baidya, M.S. Hegde, K.R. Priolkar, P.R. Sarode, Catal. Lett. 108 (2006) 165–172.
[23] M. Luo, J. Chen, L. Chen, J. Lu, Z. Feng, C. Li, Chem. Mater. 13 (2000) 197–202.
[24] B. Reddy, P. Bharali, P. Saikia, A. Khan, S. Loridant, M. Muhler, W. Grünert, J. Phys. Chem. C 111 (2007) 1878–1881.
[25] A. Gupta, M.S. Hegde, K.R. Priolkar, U.V. Waghmare, P.R. Sarode, S. Emura, Chem. Mater. 21 (2009) 5836–5847.
[26] T. Baidya, A. Gupa, P.A. Deshpandey, G. Madras, M.S. Hegde, J. Phys. Chem. C 113 (2009) 4059–4068.
[27] V.R. Choudhary, B.S. Uphade, S.G. Pataskar, Appl. Catal. A 227 (2002) 29–41.
[28] G. Saracco, G. Scibilia, A. Iannibello, G. Baldi, Appl. Catal. B 8 (1996) 229–244.
[29] E. Bekaert, L. Montagne, L. Delevoye, G. Palavit, A. Wattiaux, J. Non-Cryst. Solids 345–346 (2004) 70–74.
[30] X. Yao, Q. Yu, Z. Ji, Y. Lv, Y. Cao, C. Tang, F. Gao, L. Dong, Y. Chen, Appl. Catal. B 130–131 (2013) 293–304.
[31] X. Zhu, X. Gao, R. Qin, Y. Zeng, R. Qu, C. Zheng, X. Tu, Appl. Catal. B 170–171 (2015) 293–300.
[32] W.F. Lim, K.Y. Cheong, J. Phys. Chem. C 117 (2013) 14014–14024.
[33] A.B. Gambhire, M.K. Lande, S.B. Kalokhe, M.D. Shirsat, K.R. Patil, R.S. Gholap, B.R. Arbad, Mater. Chem. Phys. 112 (2008) 719–722.
[34] A. Leonardy, W.Z. Hung, D.S. Tsai, C.C. Chou, Y.S. Huang, Cryst. Growth Des. 9 (2009) 3958–3963.
[35] C.H. Shek, G.M. Lin, J.K.L. Lai, Nanostruct. Mater. 11 (1999) 831–835.

[36] J.E. Spanier, R.D. Robinson, F. Zhang, S.W. Chan, I.P. Herman, Phys. Rev. B 64 (2001) 245407.

[37] L. Qi, Q. Yu, Y. Dai, C. Tang, L. Liu, H. Zhang, F. Gao, L. Dong, Y. Chen, Appl. Catal. B 119/120 (2012) 308–320.

[38] K. Li, H. Wang, Y. Wei, D. Yan, Appl. Catal. B 97 (2010) 361–372.

[39] C. Li, M. Li, J. Raman Spectrosc. 33 (2002) 301–308.

[40] Z. Pu, J. Lu, M. Luo, Y. Xie, J. Phys. Chem. C 111 (2007) 18695–18702.

[41] A. Jia, G. Hu, L. Meng, Y. Xie, J. Lu, M. Luo, J. Catal. 289 (2012) 199–209.

[42] G. Laugel, J. Arichi, M. Moliere, A. Kiennemann, F. Garin, B. Louis, Catal. Today 138 (2008) 38–42.

[43] H. Arandiyan, H. Dai, J. Deng, Y. Wang, S. Xie, J. Li, Chem. Commun. 49 (2013) 10748–10750.

[44] M. Raciulete, G. Layrac, D. Tichit, I. Marcu, Appl. Catal. A 477 (2014) 195–204.

[45] M.F. Wilkes, P. Hayden, A.K. Bhattacharya, J. Catal. 219 (2003) 286–294.

[46] M. Haneda, S.I. Ohzu, Y. Kintaichi, K.I. Shimizu, J. Shibata, H. Yoshida, H. Hamada, Bull. Chem. Soc. Jpn. 74 (2001) 2075–2081.

[47] Z. Wu, J. Zhang, R.E. Benfield, Y. Ding, D. Grandjean, Z. Zhang, X. Ju, J. Phys. Chem. B 106 (2002) 4569–4577.

[48] http://srdata.nist.gov/xps/

[49] X.G. Li, Y.H. Dong, H. Xian, W.Y. Hernandez, M. Meng, H.H. Zou, A.J. Ma, T.Y. Zhang, Z. Jiang, N. Tsubaki, P. Vernoux, Energy Environ. Sci. 4 (2011) 3351–3354.

[50] M. Zhao, M. Shen, J. Wang, J. Catal. 248 (2007) 258–267.

[51] A. Katsaournis, Z. Nikopoulou, X.E. Verykios, C.G. Vayenas, J. Catal. 222 (2004) 192–206.

[52] T.H. Nguyen, A. Łamacz, A. Krztoń, A. Ura, K. Chalupka, M. Nowosielska, J. Rynkowski, G.D. Mariadassou, Appl. Catal. B 165 (2015) 389–398.

[53] T.H. Nguyen, A. Łamacz, P. Beaunier, S. Czajkowska, M. Domanski, A. Krztoń, T.V. Le, G.D. Mariadassou, Appl. Catal. B 152–153 (2014) 360–369.

[54] A. Łamacz, A. Krztoń, Int. J. Hydr. Energy 38 (2013) 8772–8782.

[55] P.M. Heynderickx, J.W. Thybaut, H. Poelman, D. Poelman, G.B. Marin, J. Catal. 272 (2010) 109–120.

[56] A. Łamacz, A. Krztoń, A. Musi, P.D. Costa, Catal. Lett. 128 (2009) 40–48.

[57] W. Li, Y. Lin, Y. Zhang, Catal. Today 83 (2009) 239–245.

[58] C. Wang, C. Chen, H. Weng, Chemosphere 57 (2004) 1131–1138.

[59] X. Xie, Y. Li, Z.Q. Liu, M. Haruta, W. Shen, Nature 458 (2009) 746–749.

[60] F. Teng, W. Han, S. Liang, B. Gauteu, R. Zong, Y. Zhu, J. Catal. 250 (2007) 1–11.